

Supporting information for

**Highly graphitized nitrogen-doped ordered mesoporous carbon  
supported Ni nanocrystals for efficient hydrazine-assisted CO<sub>2</sub>  
splitting**

*Kang Lian<sup>a,b</sup>, Junyang Ding<sup>c</sup>, Jin Zhang<sup>a\*</sup>, Quan Zhang<sup>b,c\*</sup>, Yifan Liu<sup>d</sup>, Guangzhi Hu<sup>e</sup>,  
Jia He<sup>b</sup>, and Xijun Liu<sup>c\*</sup>*

- a) *School of Public Health/Key Laboratory of Endemic and Ethnic Diseases, Ministry of Education & Key Laboratory of Medical Molecular Biology of Guizhou Province, Guizhou Medical University, Guiyang 561113, China*
- b) *Institute for New Energy Materials & Low-Carbon Technologies, School of Materials Science and Engineering, Tianjin University of Technology, Tianjin 300384, China*
- c) *Guangxi Key Laboratory of Processing for Non-ferrous Metals and Featured Materials, MOE Key Laboratory of New Processing Technology for Nonferrous Metals and Materials, School of Resources, Environment and Materials, Guangxi University, Nanning, 530004 Guangxi, China*
- d) *Institute of Advanced Science Facilities, Shenzhen 518107, Guangdong, China*
- e) *Institute for Ecological Research and Pollution Control of Plateau Lakes School of Ecology and Environmental Science, Yunnan University, Kunming 650504, China*

\*Corresponding authors: jzhang@gmc.edu.cn; 18230299580@163.com; xjliu@gxu.edu.cn

## 1 **1. Material synthesis**

2 Ni-NC is readily prepared through hard-template wet synthesis and the following pyrolytic  
3 treatment. In a typical synthesis, 0.5 g of ordered mesoporous silica (SBA-15, purchased  
4 from XFNANO) and 0.22 g of nickel chloride hexahydrate ( $\text{NiCl}_2 \cdot 6\text{H}_2\text{O}$ , bought from  
5 Aladdin) are uniformly mixed in 3.0 mL of deionized water (prepared in the laboratory).  
6 After air-drying, the resulting Ni precursor is transferred to a 50 mL round-bottom flask  
7 containing 2.0 g of ethylenediamine (EDA, obtained from Sinopharm) and 4.0 g of carbon  
8 tetrachloride (CTC, acquired from Innochem). After thorough ultrasonic dispersion, a  
9 homogeneous pink mixture is observed in the flask, which is then stirred and refluxed at 90  
10 °C for 6 hours until complete polymerization of EDA and CTC. The resulting brownish  
11 polymer is carbonized in a 900 °C argon-hydrogen mixed atmosphere (9: 1) with a heating  
12 rate of 5 °C  $\text{min}^{-1}$  for 2 hours. Finally, the carbonaceous compound is etched with 8 wt%  
13 hydrofluoric acid (HF, purchased from Aladdin) for 12 hours, washed repeatedly with  
14 deionized water, and dried to obtain Ni-NC. The synthesis of the Ni-NC-X series ( $X = 0.1,$   
15  $0.5, 1.5$ ) follows the same steps as described above, with the only variation being the amount  
16 of nickel incorporated. In the corresponding steps,  $\text{NiCl}_2 \cdot 6\text{H}_2\text{O}$  is added in amounts of 0.1  
17 (0.022 g), 0.5 (0.11 g), and 1.5 (0.33 g) times that used for Ni-NC. The synthesis of NC also  
18 follows the same steps as described above, but without the addition of  $\text{NiCl}_2 \cdot 6\text{H}_2\text{O}$ .

## 19 **2. Material Characterization**

20 Scanning electron microscopy (SEM) images were taken on a Nova NanoSEM450 scanning  
21 electron microscope. Transmission electron microscopy (TEM) measurements were  
22 performed on a JEM-ARM 200F transmission electron microscope. Powder X-ray diffraction

23 (XRD) patterns were obtained by an X-ray diffractometer (Rigaku SmartLab) at a scan rate of  
24  $10^\circ \text{ min}^{-1}$  with Cu  $K\alpha$  radiation ( $\lambda = 0.154598 \text{ nm}$ ). Raman spectrum was recorded on a  
25 Raman microscope of Horiba Evolution.  $\text{N}_2$  adsorption-desorption isotherms were measured  
26 on an Autosorb-IQ3+ChemStar. Specific surface areas were calculated by the Brunauer-  
27 Emmett-Teller (BET) method and pore sizes were obtained by a non-local density functional  
28 theory (NLDFT) method. X-ray photoelectron spectroscopy (XPS) was collected by a  
29 Thermo Scientific ESCALAB250Xi photoelectron spectrometer equipped with the Al  $K\alpha$   
30 (1486.6 eV) radiation as the X-ray source and the C 1s peak was fixed at the binding energy  
31 of 284.8 eV.

### 32 **3. Electrochemical measurements**

33 All electrochemical tests were performed at room temperature using a CHI760e  
34 electrochemical workstation. Linear sweep voltammetry (LSV) curves were recorded at a  
35 scan rate of  $5 \text{ mV s}^{-1}$  without infrared compensation. Current densities were calculated based  
36 on the geometric area of the working electrode and were normalized to the reversible  
37 hydrogen electrode (RHE).

#### 38 **3.1 *CO<sub>2</sub>RR measurements***

39 Typical  $\text{CO}_2$  reduction reaction ( $\text{CO}_2\text{RR}$ ) was conducted using a closed H-type cell  
40 separated by a proton exchange membrane (Nafion 115). Both compartments were filled with  
41  $0.5 \text{ M KHCO}_3$  aqueous solution as the electrolyte. The Ag/AgCl electrode and Pt foil were  
42 used as reference electrode and counter electrode, respectively. The working electrode was  
43 prepared by applying ink (e.g., Ni-NC or NC) onto hydrophobic carbon paper to achieve a  
44 loading of  $1 \text{ mg cm}^{-2}$ . Prior to the experiment, the electrolyte in the cathode compartment

45 was saturated with CO<sub>2</sub>/Ar. All potential for CO<sub>2</sub>RR were converted according to the  
46 following equation:

$$47 \quad E_{\text{RHE}} = E_{\text{Ag/AgCl}} + 0.0591 \times pH + 0.197 \quad \text{Eq. S1}$$

48 where *pH* of the CO<sub>2</sub>-saturated 0.5 M KHCO<sub>3</sub> was determined as 7.32.

### 49 **3.2 HzOR measurements**

50 The hydrazine oxidation reaction (HzOR) and water oxidation reaction (OER) were  
51 conducted using a single-pool reactor, with electrolytes consisting of 1 M KOH with 0.5 M  
52 N<sub>2</sub>H<sub>4</sub> solution and 1 M KOH solution, respectively. The Hg/HgO electrode and carbon rod  
53 were employed as reference and counter electrodes, respectively. The preparation of the  
54 working electrode was analogous to that used in CO<sub>2</sub>RR, except that hydrophilic carbon  
55 paper was selected for its fabrication. During HzOR durability testing, the electrolyte was  
56 periodically refreshed to ensure a sufficient supply of N<sub>2</sub>H<sub>4</sub>. All potential of HzOR and OER  
57 were calculated according to the following equation:

$$58 \quad E_{\text{RHE}} = E_{\text{Hg/HgO}} + 0.059 \times pH + 0.098 \quad \text{Eq. S2}$$

59 where *pH* of HzOR and OER were determined as 13.88.

### 60 **3.3 HECR measurements**

61 For the energy-efficient coupling of HzOR with CO<sub>2</sub>RR (HzOR||CO<sub>2</sub>RR), the process  
62 was conducted in a two-electrode sealed H-type cell equipped with a bipolar membrane. The  
63 anode and cathode were prepared similarly to the working electrodes used in HzOR and  
64 CO<sub>2</sub>RR. Anode chamber employed an electrolyte of 1 M KOH with 0.5 M N<sub>2</sub>H<sub>4</sub>, while the  
65 cathode chamber used 0.5 M KHCO<sub>3</sub> solution. During durability testing, the anode  
66 electrolyte was periodically refreshed to ensure a sufficient supply of N<sub>2</sub>H<sub>4</sub>. For comparison,

67 a traditional water oxidation-coupled CO<sub>2</sub>RR (OER||CO<sub>2</sub>RR) anode utilized 1 M KOH  
68 solution as the electrolyte. Compared to OER||CO<sub>2</sub>RR, the energy saving efficiency ( $\eta$ ) for  
69 energy-efficient HzOR||CO<sub>2</sub>RR was calculated based on the required voltages of the full cell  
70 from the following equation <sup>1</sup>:

$$71 \eta = (E_{\text{OER}||\text{CO}_2\text{RR}} - E_{\text{HzOR}||\text{CO}_2\text{RR}}) / E_{\text{OER}||\text{CO}_2\text{RR}} \times 100\% \quad \text{Eq. S3}$$

72 Further evaluation of the HzOR||CO<sub>2</sub>RR system is conducted within a membrane  
73 electrode assembly (MEA). The catalyst layer, with a loading of 1 mg cm<sup>-2</sup>, is tightly  
74 deposited on both sides of the anion exchange membrane, with stable titanium felt serving as  
75 the anode, and a gas diffusion electrode, formed by hydrophobic carbon paper, functioning as  
76 the cathode. The anode chamber employs an electrolyte consisting of a 1 M KOH solution  
77 containing 0.5 M N<sub>2</sub>H<sub>4</sub>, whereas the cathode chamber is supplied with humidified CO<sub>2</sub>. In  
78 contrast, the conventional OER||CO<sub>2</sub>RR configuration utilizes a 1 M KOH solution at the  
79 anode, with the remaining setup mirroring that of the HzOR||CO<sub>2</sub>RR.

### 80 **3.4 EIS and ECSA measurements**

81 EIS was performed at an open-circuit potential state in the frequency range from 1000  
82 kHz to 0.1 Hz with a voltage amplitude of 5 mV. To determine the double-layer capacitance  
83 ( $C_{\text{dl}}$ ) of the material within the non-Faradaic potential range, measurements were conducted  
84 at various scan rates. The electrochemical surface area (ECSA) was calculated using the  
85 following equation:

$$86 R_f = C_{\text{dl}} / C_s \quad \text{Eq. S4}$$

$$87 \text{ECSA} = R_f \times S \quad \text{Eq.}$$

88 S5

89 where  $R_f$  is the roughness factor,  $C_s$  is the specific capacitance of the carbon-based support  
90 ( $1.03 \text{ mF cm}^{-2}$ )<sup>2</sup>.  $S$  is the geometric active area ( $1 \times 1 \text{ cm}^2$ ).

### 91 **3.5 TOF measurements**

92 TOF values were calculated according to the previously reported equation<sup>3,4</sup>:

$$93 \text{ TOF} = (j \times S) / (\alpha \times F \times n) \quad \text{Eq.}$$

94 **S6**

95 where  $j$  is the HzOR current density;  $S$  is the geometric active area ( $1 \times 1 \text{ cm}^2$ );  $\alpha$  is 4 for  
96 HzOR; and  $F$  is the Faraday constant ( $96485 \text{ C mol}^{-1}$ ). The  $n$  values were measured by a  
97 widely used

98 method<sup>5</sup>: Cyclic voltammetry (CV) measurements were performed when the scan rate was  
99 fixed at  $50 \text{ mV s}^{-1}$ . After this, by integrating the charge of CV curve over the whole potential  
100 range, the half value of the charge was obtained, which is the value of the surface charge  
101 density ( $Q_s$ ). Then, the  $n$  value was calculated using the following equation:

$$102 n = Q_s / F \quad \text{Eq.}$$

103 **S7**

104 where  $F$  is the Faraday constant ( $96485 \text{ C mol}^{-1}$ ).

### 105 **4. Product analysis**

106 Gaseous products of  $\text{CO}_2\text{RR}$  were monitored by a gas chromatograph (GC, Agilent 7890B)  
107 equipped with a flame ionization detector (FID) and thermal conductivity detector (TCD).

108 Electrolyte solution was collected from the cathode chamber after electrolysis and  
109 characterized by Avance III HD 400MHz  $^1\text{H}$  nuclear magnetic resonance ( $^1\text{H NMR}$ ). Faraday

110 efficiency of CO ( $\text{FE}_{\text{CO}}$ ) was calculated as the following equation:

111  $FE_{CO} = (2 \times m \times F)/Q = (2 \times C_{gas} \times V_{CO_2} \times 10^{-3} \times t \times F)/(24.8 \times Q)$  Eq. S8

112 where  $m$  is the mol amount of CO;  $F$  is the Faraday constant (96485 C mol<sup>-1</sup>);  $Q$  is the total  
113 quantity of electric charge during the CO<sub>2</sub>RR at a constant current density;  $C_{gas}$  is the volume  
114 concentration of the gas products, originating from the GC;  $V_{CO_2}$  is the flow rate of CO<sub>2</sub> (30  
115 mL min<sup>-1</sup>);  $t$  is electrolysis time.

## 116 **5. In situ FTIR measurements**

117 In situ fourier transform infrared (In situ FTIR) were recorded using a Bruker FTIR  
118 spectrometer (CRCP-7070-A). A gilded silicon hemispherical prism served as both the  
119 conductive substrate and the infrared reflection element, while the Ni-NC was deposited on  
120 the Au/Si surface to function as the working electrode. For CO<sub>2</sub>RR, Ag/AgCl and Pt wire  
121 were utilized as the reference and counter electrodes, respectively, while the electrolyte  
122 consisted of a CO<sub>2</sub>-saturated 0.5 M KHCO<sub>3</sub> solution. For the HzOR, a Hg/HgO electrode  
123 served as the reference electrode, and a carbon rod was used as the counter electrode, with a 1  
124 M KOH solution containing 0.5 M N<sub>2</sub>H<sub>4</sub> as the electrolyte. During the progressive potential  
125 of the working electrode, spectral signals were collected at a resolution of 4 cm<sup>-1</sup>, with 20  
126 scans performed for each applied potential.

## 127 **6. DFT calculations**

128 All density functional theory (DFT) calculations were performed using the Vienna Ab initio  
129 Simulation Package (VASP). For the treatment of electronic exchange and correlation effects,  
130 the Perdew-Burke-Ernzerhof exchange-correlation functional, based on the generalized  
131 gradient approximation, was employed. The kinetic energy cutoffs for the plane-wave basis  
132 set were fixed at 500 eV to ensure accurate energy convergence. The Brillouin zone was

133 sampled with a  $1 \times 1 \times 1$  k-point grid across all computational models to achieve sufficient  
134 precision. A vacuum region of 20 Å was introduced along the Z-axis to minimize spurious  
135 interactions between periodic images. The convergence thresholds were rigorously set to  $10^{-5}$   
136 eV for electronic self-consistency and 0.05 eV Å<sup>-1</sup> for ionic relaxation. The free energy  
137 change ( $\Delta G$ ) of each adsorbed intermediate was computed using the following expression:

$$138 \quad \Delta G = \Delta E + \Delta ZPE - T\Delta S \quad \text{Eq. S9}$$

139 Where  $\Delta E$ ,  $\Delta ZPE$  and  $\Delta S$  represent the changes in electronic energy, zero-point energy, and  
140 entropy associated with the adsorption of intermediates, respectively. The thermodynamic  
141 corrections at the reaction temperature (298 K) were calculated using the VASPKit software  
142 suite.



## Figures and Tables

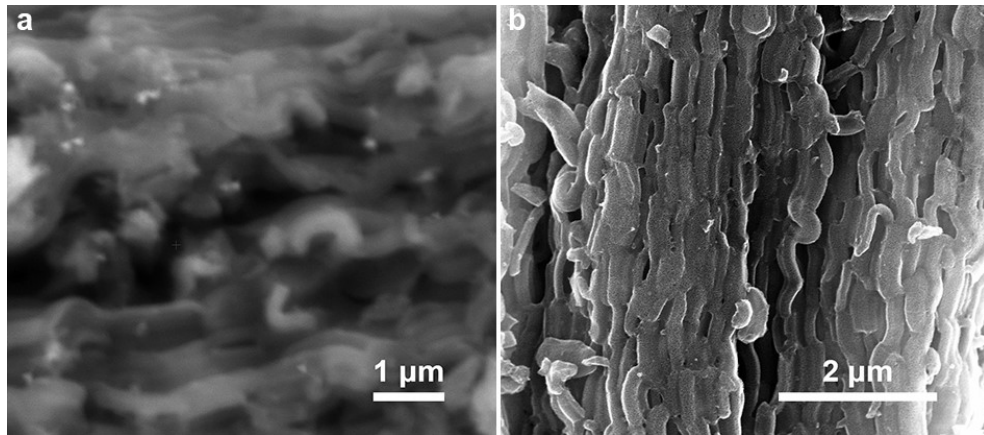


**Fig. S1.** SEM images of a) Ni-NC and b) NC.

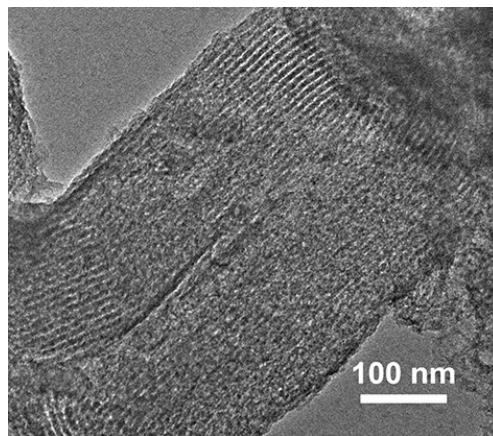


**Fig. S2.** TEM image of NC.

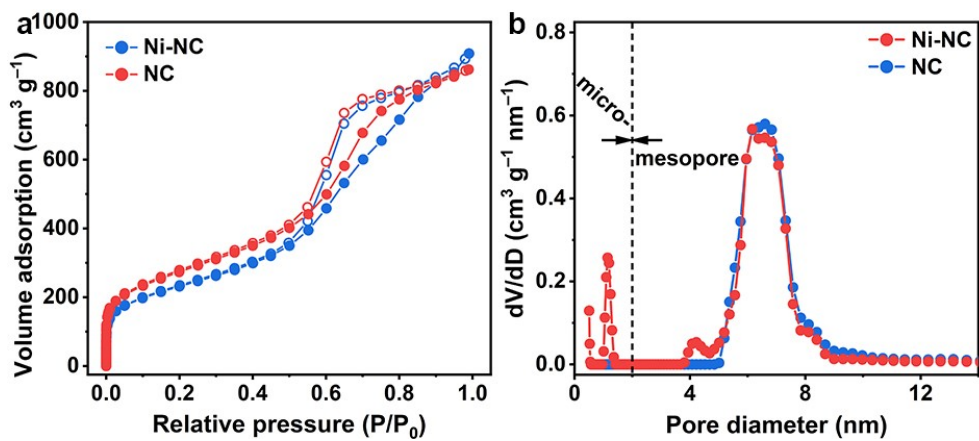


**Fig. S3.** a)  $N_2$  adsorption-desorption isotherm curves, and b) Corresponding pore size distribution of Ni-NC and NC.

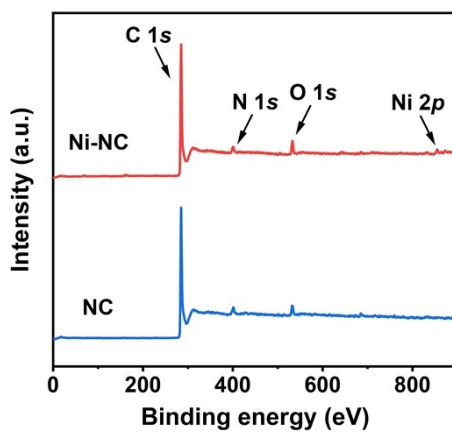


**Fig. S4.** Comparison referring to the XPS survey spectra of Ni-NC and NC.

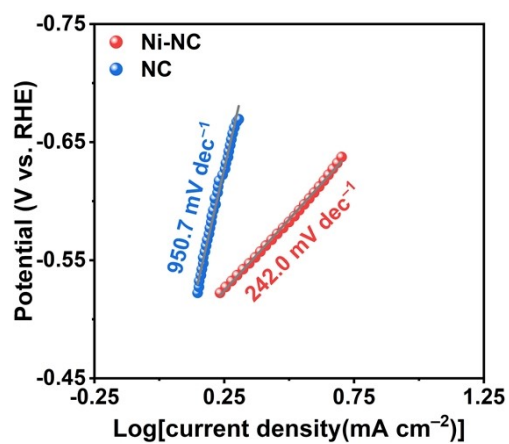


**Fig. S5.** Tafel slope of Ni-NC and NC under CO<sub>2</sub>-saturated condition in 0.5 M KHCO<sub>3</sub>.

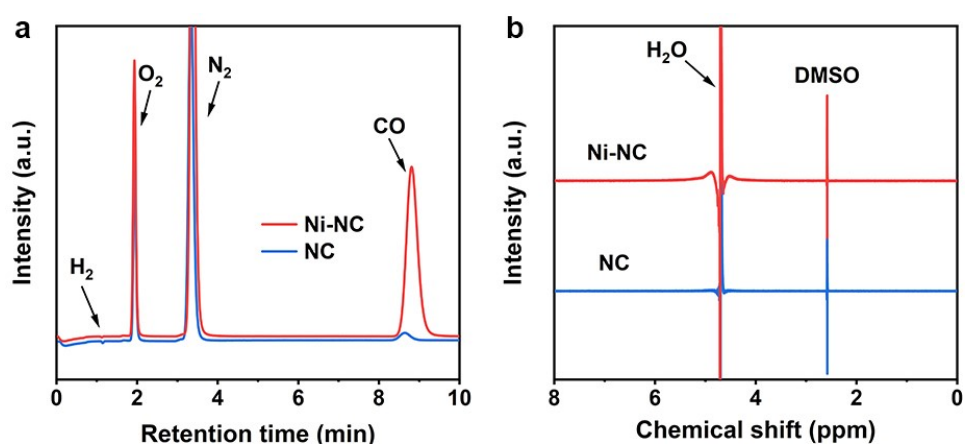


**Fig. S6.** a) GC's TCD channels of the CO<sub>2</sub>RR gas products for Ni-NC and NC at 1.0 V vs. RHE, and b) Corresponding <sup>1</sup>H NMR spectra of the CO<sub>2</sub>RR liquid products for Ni-NC and NC after electrolysis.

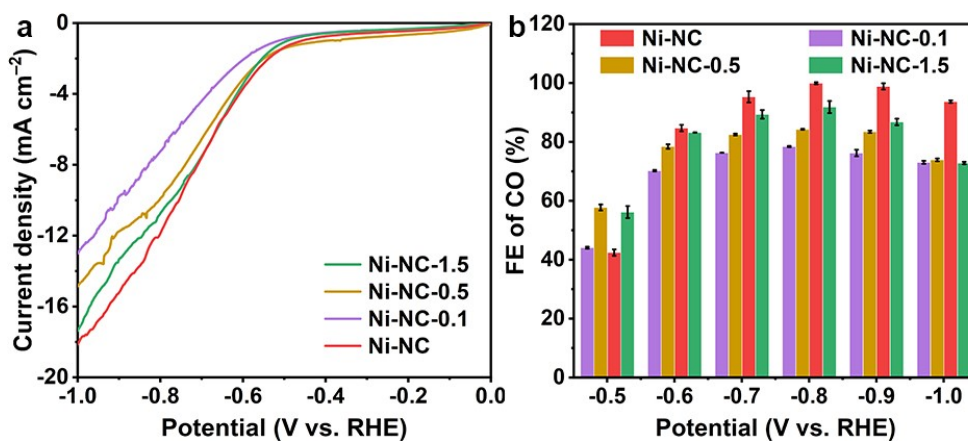


**Fig. S7.** a) LSV curves and b) FE<sub>CO</sub> of Ni-NC and Ni-NC-X (X = 0.1, 0.5, and 1.5) under CO<sub>2</sub>-saturated condition in 0.5 M KHCO<sub>3</sub>.

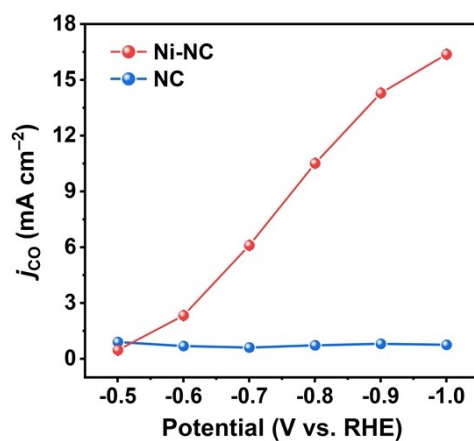


**Fig. S8.** Calculated  $j_{CO}$  of Ni-NC and NC in CO<sub>2</sub>RR tests.

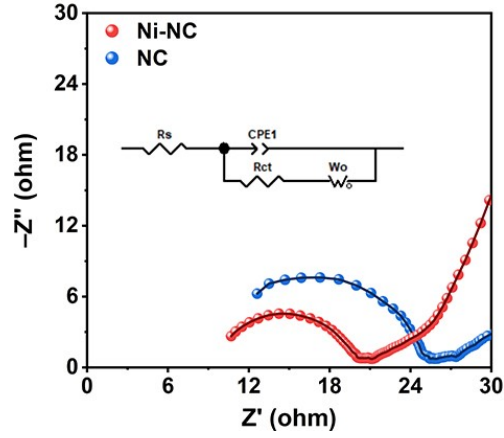


Fig. S9. EIS analysis of Ni-NC and NC in CO<sub>2</sub>RR tests.

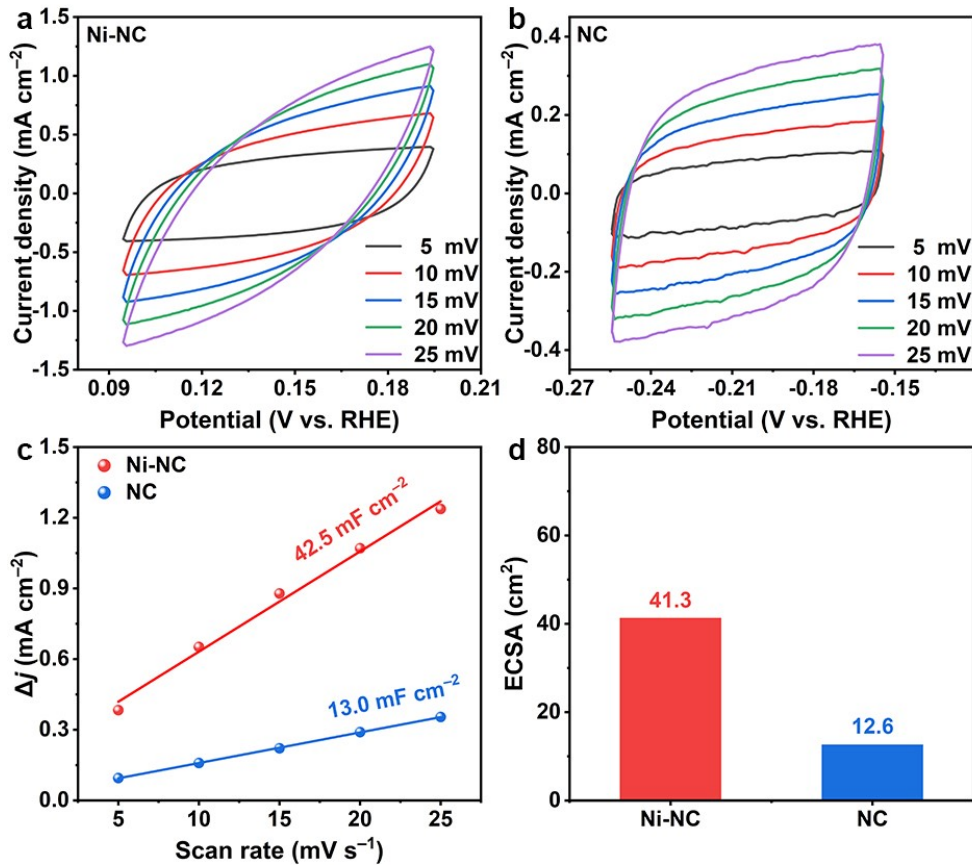
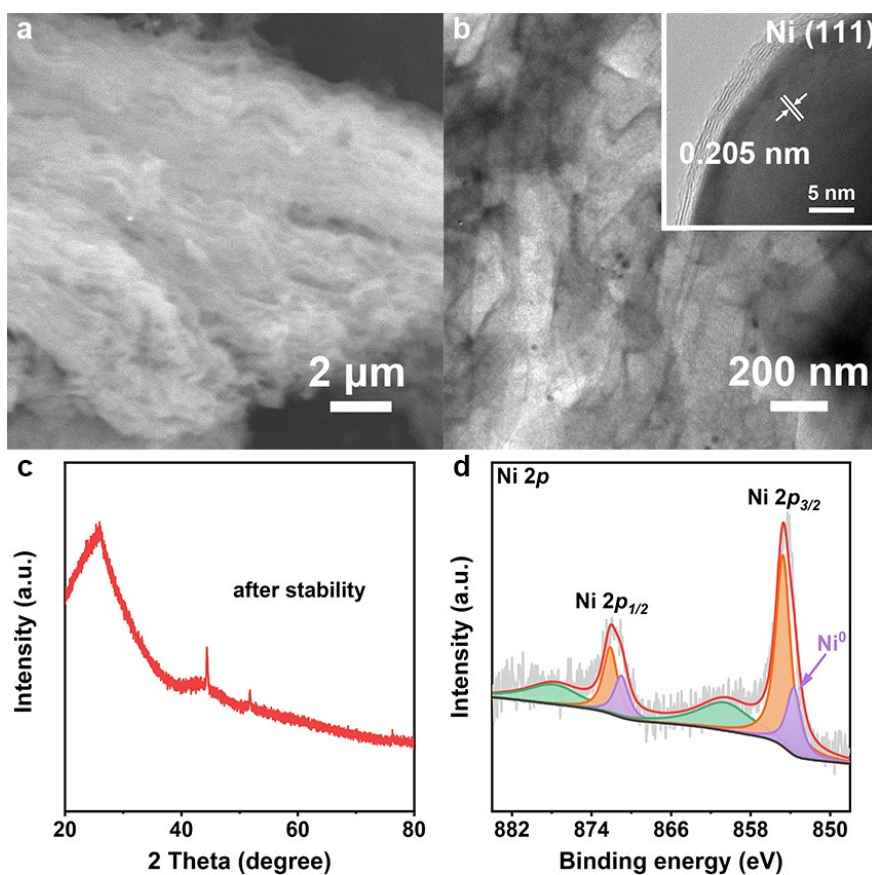


Fig. S10. CVs of a) Ni-NC and b) NC measured in non-Faradaic regions at scan rates of 5 – 25 mV s<sup>-1</sup> in

CO<sub>2</sub>RR tests, and corresponding c)  $C_{dl}$  and d) ECSA of Ni-NC and NC.



**Fig. S11.** a) SEM, b) TEM, c) XRD, and d) XPS of Ni 2p for Ni-NC after CO<sub>2</sub>RR stability test. Inset in b):

locally magnified TEM images of Ni NCs.

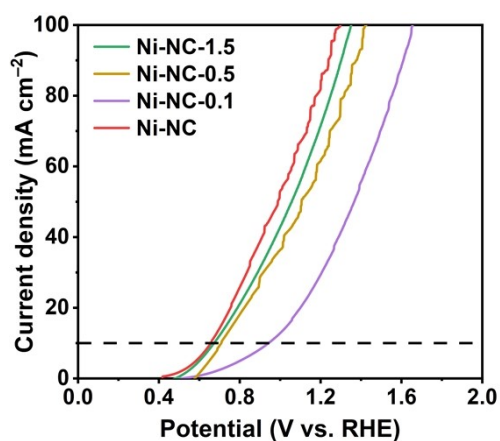


**Fig. S12.** LSV curves of Ni-NC and Ni-NC-X (X = 0.1, 0.5, and 1.5) in 1 M KOH with 0.5 M N<sub>2</sub>H<sub>4</sub>.

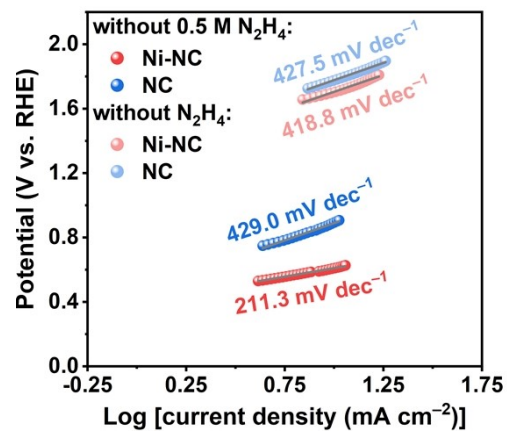


**Fig. S13.** Tafel slope of Ni-NC and NC in 1 M KOH with and without 0.5 M N<sub>2</sub>H<sub>4</sub>.

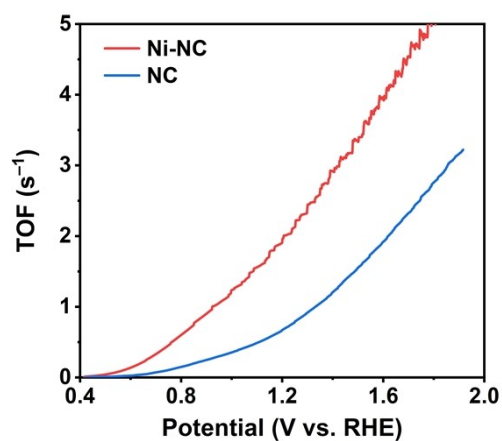


**Fig. S14.** TOF curves of Ni-NC and NC were derived from the LSV curves.

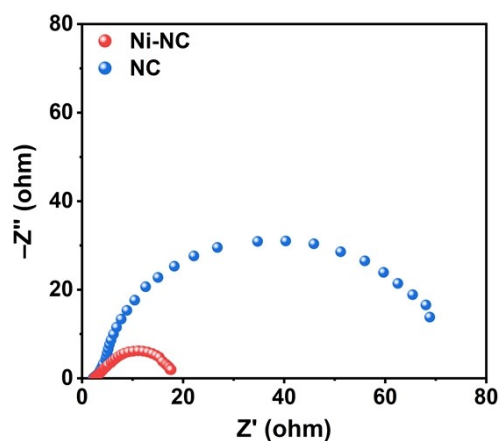


Fig. S15. EIS analysis of Ni-NC and NC in HzOR tests.

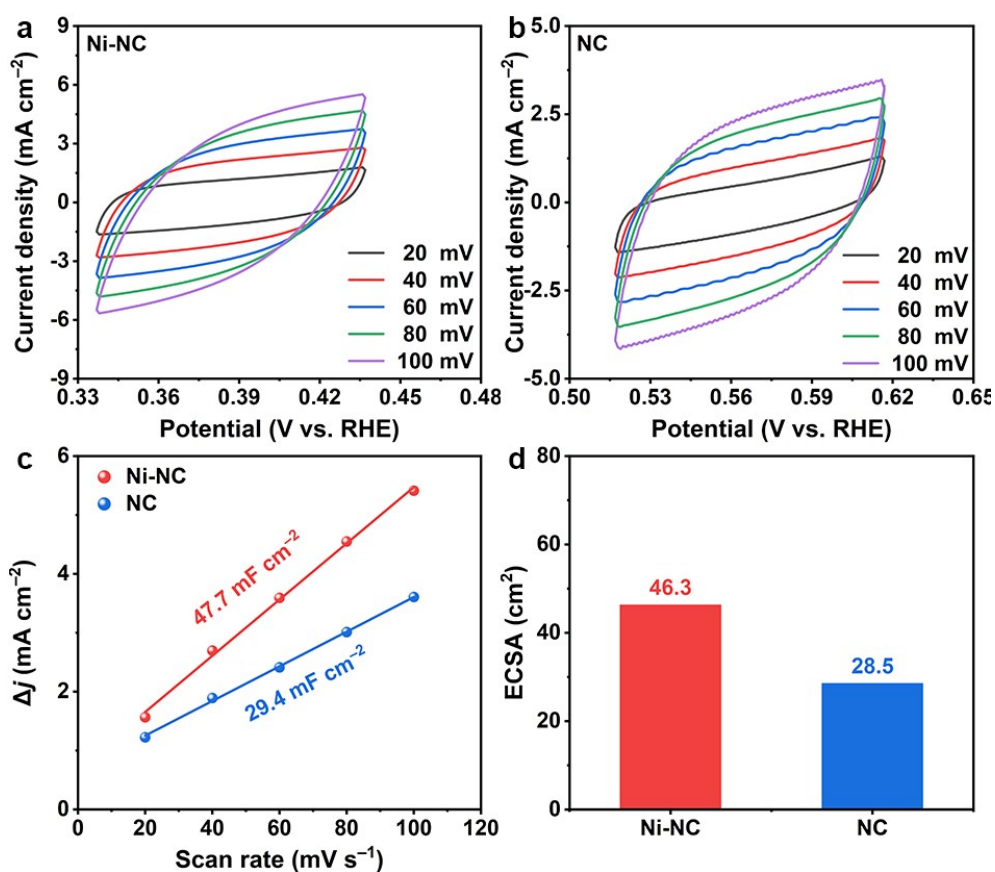
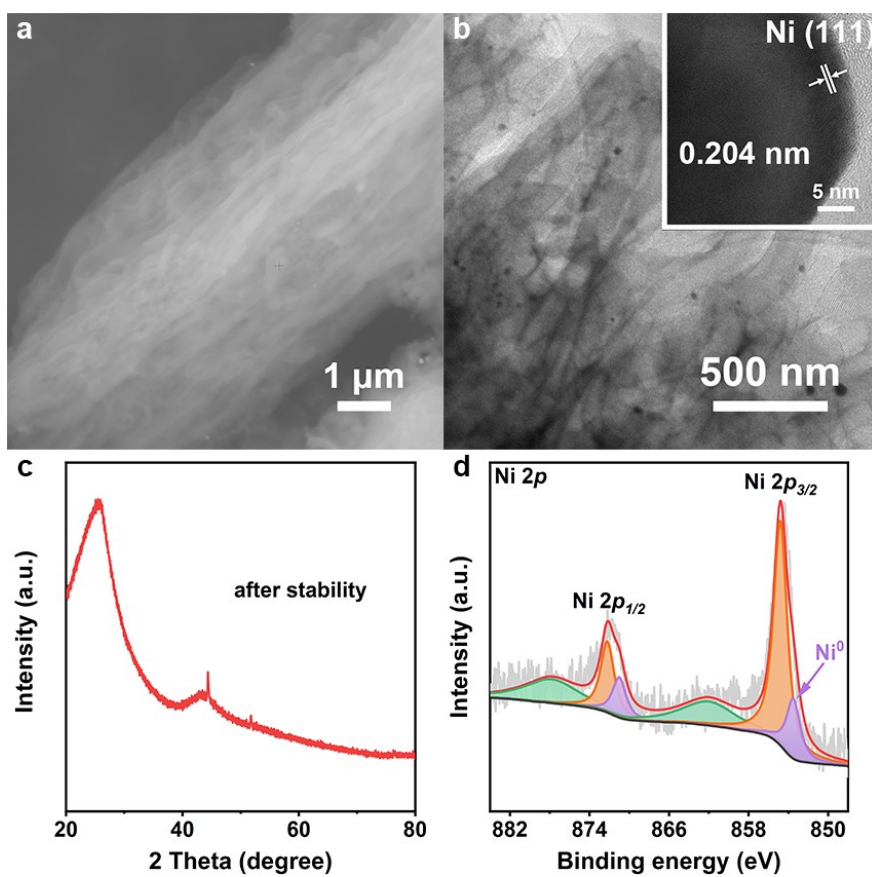


Fig. S16. CVs of a) Ni-NC and b) NC measured in non-Faradaic regions at scan rates of 20 – 100  $\text{mV s}^{-1}$

in HzOR tests, and corresponding c)  $C_{dl}$  and d) ECSA of Ni-NC and NC.





**Fig. S17.** a) SEM, b) TEM, c) XRD, and d) XPS of Ni  $2p$  for Ni-NC after HzOR stability test. Inset in b):

locally magnified TEM images of Ni NCs.

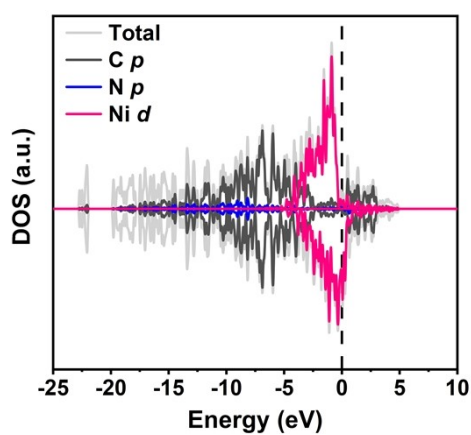


**Fig. S18.** Density of states for Ni-NC.

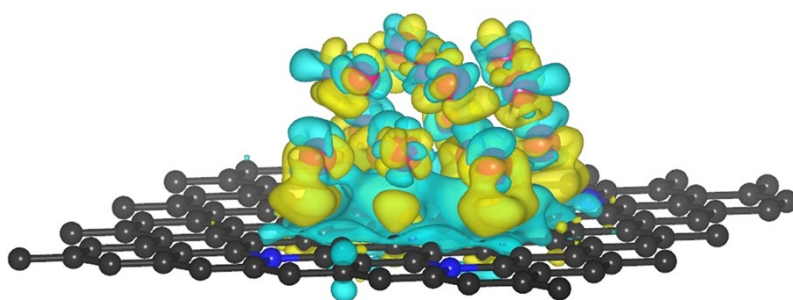


**Fig. S19.** Differential charge density of Ni-NC (the cyan and yellow areas represent charge consumption and accumulation).

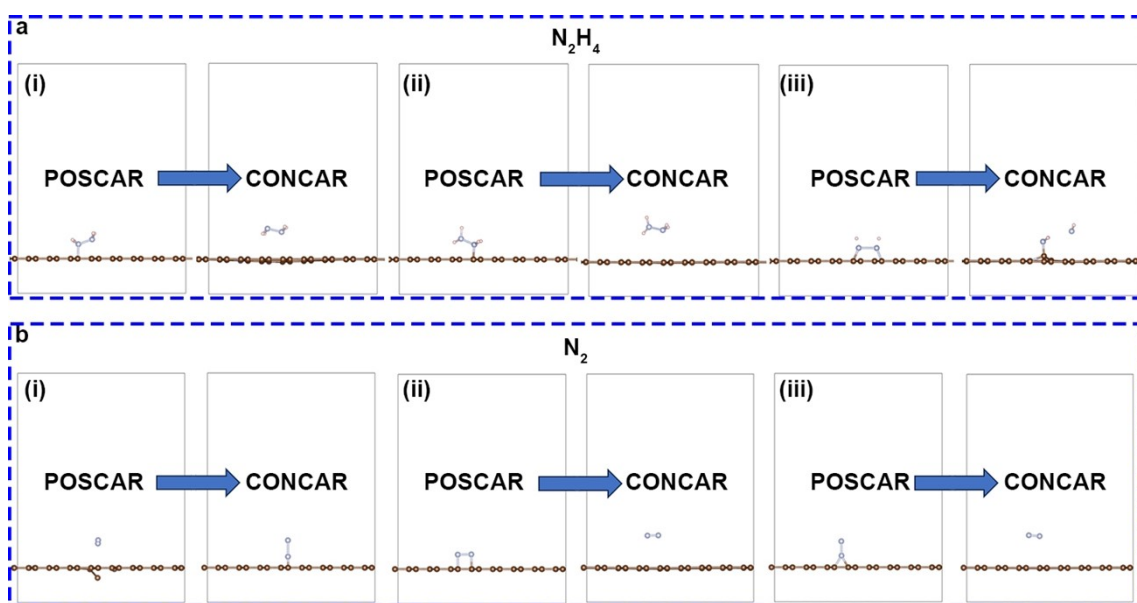


**Fig. S20.** A comparison of the pre- and post-optimization of several NC adsorption models for a)  $N_2H_4$  and b)  $N_2$ .

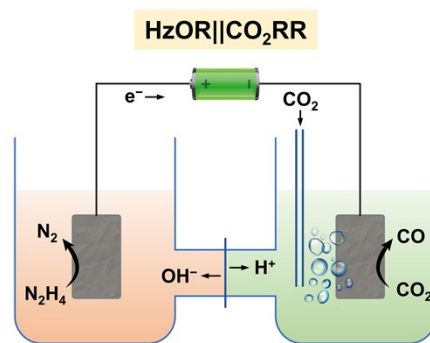


**Fig. S21.** Schematic illustration of HzOR||CO<sub>2</sub>RR in a H-type cell.

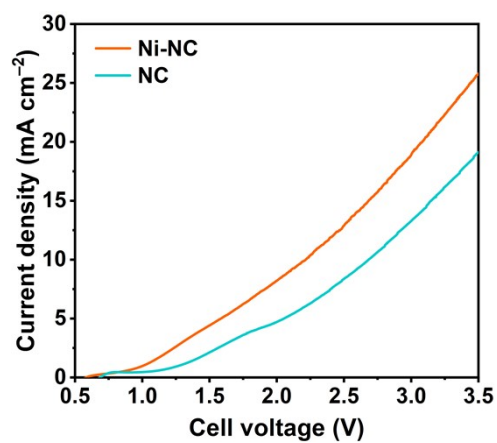


**Fig. S22.** Polarization curves of Ni-NC-based and NC-based HzOR||CO<sub>2</sub>RR.

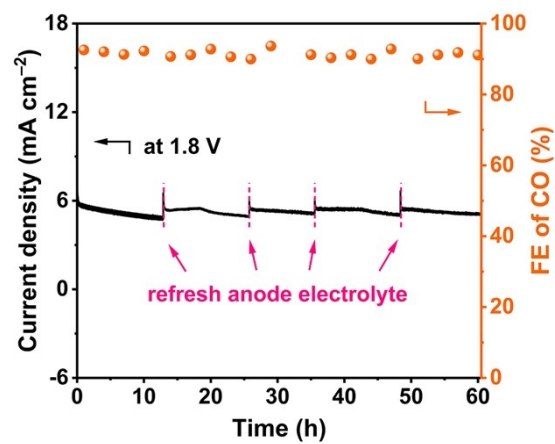


**Fig. S23.** Stability of Ni-NC for HzOR||CO<sub>2</sub>RR in the H-type cell at 1.8 V cell voltage.

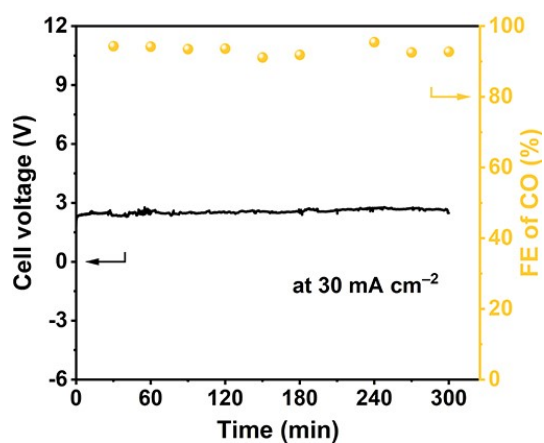


**Fig. S24.** Stability of Ni-NC for HzOR||CO<sub>2</sub>RR in the MEA at 30 mA cm<sup>-2</sup>.

**Table S1.** Comparison of specific surface areas and average pore sizes of Ni-NC and NC.

Sample	BET surface area (m <sup>2</sup> g <sup>-1</sup> )	DFT pore width (nm)
Ni-NC	827.3	6.2
NC	816.5	6.6

**Table S2.** Comparison of the reported catalysts with the Ni-NC for CO<sub>2</sub> electroreduction to CO in H-type cell.

Sample	Electrolyte	Potential <sup>[a]</sup> (V vs. RHE)	FE of CO <sup>[b]</sup> (%)	<i>j</i> <sub>CO</sub> <sup>[c]</sup> (%)	Ref.
Ni-NC	0.5 M KHCO <sub>3</sub>	-1.0	94	16.4	<b>This work</b>
FeN <sub>4</sub> /C	0.1 M KHCO <sub>3</sub>	-0.6	97	6.87	6
HIE/Ni-N-C	0.5 M KHCO <sub>3</sub>	-1.0	97	13	7
Ni/NC_PAN_950	0.1 M KHCO <sub>3</sub>	-0.9	96.5	4.3	8
NiO/Ni-N-C-800	0.1 M KHCO <sub>3</sub>	-1.0	92	10	9
NC-CNTs (Ni)	0.1 M KHCO <sub>3</sub>	-1.0	90	10	10
Ni-N-C	0.1 M KHCO <sub>3</sub>	-1.0	85	17	11
Ni-N <sub>x</sub> -C <sub>2</sub>	0.1 M KHCO <sub>3</sub>	-0.7	85	9.5	12
Ni-N-Gr	0.1 M KHCO <sub>3</sub>	-1.0	85	3.3	13
ACP/S-N-Ni	0.5 M KHCO <sub>3</sub>	-0.77	80	3.4	14
CNS-NiSA	0.5 M KHCO <sub>3</sub>	-1.0	74	11	15
Ni-N-C	0.1 M KHCO <sub>3</sub>	-0.8	69	1	16
Ni-NG	0.5 M KHCO <sub>3</sub>	-1.0	60	9	17

[a-c] Data were directly obtained from the literature or calculated from the given data.

## References

- 1 C. Hu, Y. Zhang, A. Hu, Y. Wang, X. Wei, K. Shen, L. Chen and Y. Li, *Adv. Mater.*, 2023, **35**, 2209298.
- 2 X. Zhang, W. Shen, Z. Li, D. Wang, J. Qi and C. Liang, *Carbon*, 2020, **167**, 548–558.
- 3 X. Liu, J. He, S. Zhao, Y. Liu, Z. Zhao, J. Luo, G. Hu, X. Sun and Y. Ding, *Nat. Commun.*, 2018, **9**, 4365.
- 4 C. Tang, R. Zhang, W. Lu, Z. Wang, D. Liu, S. Hao, G. Du, A. M. Asiri and X. Sun, *Angew. Chem. Int. Ed.*, 2017, **56**, 842–846.
- 5 D. Merki, S. Fierro, H. Vrubel and X. Hu, *Chem. Sci.*, 2011, **2**, 1262–1267.
- 6 C. Liu, Y. Wu, K. Sun, J. Fang, A. Huang, Y. Pan, W. Cheong, Z. Zhuang, Z. Zhuang, Q. Yuan, H. L. Xin, C. Zhang, J. Zhang, H. Xiao, C. Chen and Y. Li, *Chem*, 2021, **7**, 1297–1307.
- 7 Y. Kong, A. Zheng, Z. Wu, Q. Chen and X. Hu, *Mater. Today Chem.*, 2023, **28**, 101386.
- 8 M. Zhang, T. Wu, S. Hong, Q. Fan, Y. Soo, J. Masa, J. Qiu and Z. Sun, *ACS Sustain. Chem. Eng.*, 2019, **7**, 15030–15035.
- 9 H. Li, K. Gan, R. Li, H. Huang, J. Niu, Z. Chen, J. Zhou, Y. Yu, J. Qiu and X. He, *Adv. Funct. Mater.*, 2022, **33**, 2208622.
- 10 Q. Fan, P. Hou, C. Choi, T. Wu, S. Hong, F. Li, Y. Soo, P. Kang, Y. Jung and Z. Sun, *Adv. Energy Mater.*, 2019, **10**, 1903068.
- 11 F. Pan, H. Zhang, Z. Liu, D. Cullen, K. Liu, K. More, G. Wu, G. Wang and Y. Li, *J. Mater. Chem. A*, 2019, **7**, 26231–26237.
- 12 W. Ju, A. Bagger, G. P. Hao, A. S. Varela, I. Sinev, V. Bon, B. Roldan Cuenya, S.

- Kaskel, J. Rossmeisl and P. Strasser, *Nat. Commun.*, 2017, **8**, 944.
- 13 P. Su, K. Iwase, S. Nakanishi, K. Hashimoto and K. Kamiya, *Small*, 2016, **12**, 6083–6089.
- 14 S. Li, M. Ceccato, X. Lu, S. Frank, N. Lock, A. Roldan, X. Hu, T. Skrydstrup and K. Daasbjerg, *J. Mater. Chem. A*, 2021, **9**, 1583–1592.
- 15 X. Zhao, S. Huang, Z. Chen, C. Lu, S. Han, C. Ke, J. Zhu, J. Zhang, D. Tranca and X. Zhuang, *Carbon*, 2021, **178**, 488–496.
- 16 B. J. Park, Y. Wang, Y. Lee, K. J. Noh, A. Cho, M. G. Jang, R. Huang, K. S. Lee and J. W. Han, *Small*, 2021, **17**, e2103705.
- 17 K. Jiang, S. Siahrostami, T. Zheng, Y. Hu, S. Hwang, E. Stavitski, Y. Peng, J. Dynes, M. Gangisetty, D. Su, K. Attenkofer and H. Wang, *Energy Environ. Sci.*, 2018, **11**, 893–903.